



Cite this: *RSC Adv.*, 2023, 13, 9010

# Distinct morphology-dependent behaviors for Au/ $\gamma$ -Al<sub>2</sub>O<sub>3</sub> catalysts: enhanced thermal stabilization in CO oxidation reaction

Weimeng Cai,<sup>†</sup> Xinyu Sun,<sup>†</sup> Yaojie Bao, Jianhua Guo, Anqiu Liu, Kunhong Hu\* and Lipin Feng \*

The durability of supported metal catalysts usually suffers from sintering, the metal nanoparticles aggregating into larger sizes and subsequent loss of reactive surface, resulting in catalysts deactivation when heated at elevated temperatures. Herein, we investigate the evolution of Au species on different morphologies of  $\gamma$ -Al<sub>2</sub>O<sub>3</sub> and surprisingly found vastly different behavior for the dispersion of surface Au nanoparticles. A nanorod-shaped  $\gamma$ -Al<sub>2</sub>O<sub>3</sub> is prepared by the hydrothermal method resulting in an extraordinary catalyst support that can stabilize Au nanoparticles at annealing temperatures up to 700 °C. In contrast, the Au-supported catalyst prepared using commercial  $\gamma$ -Al<sub>2</sub>O<sub>3</sub> shows a greater degree of inactivation under the same conditions. Remarkably, the unique morphology of such nanorod-shaped  $\gamma$ -Al<sub>2</sub>O<sub>3</sub> is beneficial in preventing Au nanoparticles from sintering. The  $\gamma$ -Al<sub>2</sub>O<sub>3</sub> nanorods are more effective than the commercial  $\gamma$ -Al<sub>2</sub>O<sub>3</sub> at anchoring the Au nanoparticles. The results of X-ray photoelectron spectroscopy (XPS), *in situ* diffuse reflectance infrared Fourier transform spectroscopy (DRIFTS) and H<sub>2</sub>-TPR, reveal the interfacial interactions between Au nanoparticles and  $\gamma$ -Al<sub>2</sub>O<sub>3</sub> nanorods, yielding a sinter-stability of the obtained Au/ $\gamma$ -Al<sub>2</sub>O<sub>3</sub> nanorods catalyst. This synthetic strategy is simple and amenable to the large-scale manufacture of thermally stable  $\gamma$ -Al<sub>2</sub>O<sub>3</sub> for industrial applications. Here, we investigate the morphology-dependent behavior of Au nanoparticles dispersed on different morphologies of  $\gamma$ -Al<sub>2</sub>O<sub>3</sub>. The result of X-ray photoelectron spectroscopy (XPS), *in situ* diffuse reflectance infrared Fourier transform spectroscopy (DRIFTS) and H<sub>2</sub>-TPR, reveal the interfacial interactions between Au nanoparticles and gamma alumina nanorods. Au nanoparticles on  $\gamma$ -Al<sub>2</sub>O<sub>3</sub> nanorods exhibit higher sinter-resistant performance than those on commercial  $\gamma$ -Al<sub>2</sub>O<sub>3</sub>.

Received 14th January 2023  
Accepted 2nd March 2023

DOI: 10.1039/d3ra00272a

rsc.li/rsc-advances

## 1 Introduction

Currently, supported metal catalysts perform a vital role in both the petrochemical and environmental field, such as catalytic reforming,<sup>1</sup> catalytic hydrogenation,<sup>2</sup> cleaning of automobile exhausts,<sup>3</sup> and activation of nitrogen and methane.<sup>4</sup> Of these, carbon monoxide is one of the most widespread and deadly pollutants in industrial and vehicle exhaust emissions.<sup>5</sup> CO oxidation is of great importance in both basic research and practical applications. Oxide-loaded noble metal catalysts are also recognized as excellent CO oxidation catalysts.<sup>6</sup> From there, such catalysts have been extensively applied in industrial or pollutant treatment processes.<sup>7–10</sup> In most cases, due to the comparatively low Tammann temperature (Kelvin degrees, half of the bulk melting point) of the metal,<sup>11</sup> the metal on the surface of the supported metal catalyst has liquid-like

characteristics, exhibits a strong migration ability, and is easy to aggregate and sintering at high temperatures, thereby altering the catalytic performance.<sup>12–14</sup> The regeneration of such catalysts requires a lot of material and financial resources, especially for the supported noble metal catalysts. Therefore, understanding the sintering process of metal and the preparation of durable supported metal catalysts has significant research and application value.

In recent years, much effort has been devoted to developing new strategies for stabilizing metal nanoparticles. Recent developments in the preparation of sinter-resistant supported metal nanoparticle catalysts can be roughly divided into the following two categories: (i) strong metal-support interactions (SMSI). The intrinsic reason for sintering is ascribed to the weak interaction between metal particles and supports;<sup>15</sup> hence, the SMSI effect can improve the anti-sintering performance of the catalyst. After the SMSI formation, the geometric and electronic effects of metal nanoparticles can be modified, which involves encapsulating the metal nanoparticles with oxide overlayers, electronic interaction between metal nanoparticles and oxide, etc. TiO<sub>2</sub> (ref. 16–18) and CeO<sub>2</sub> (ref. 19–21) are two of the most

School of Energy Materials and Chemical Engineering, Hefei University, Hefei, 99 Jinxiu Rd, Hefei 230601, Anhui, People's Republic of China. E-mail: chemhu@hfuu.edu.cn; fenglipin2022@163.com; Tel: +86-551-62158315

<sup>†</sup> These authors contribute equally to this research.



extensively investigated supports for the SMSI, due to their redox behavior and oxygen storage capacity.<sup>22–24</sup> Notably, many industrially supported metal catalysts are on inert supports such as porous carbon or alumina. The SMSI strategy seems to be ineffective for these catalysts. Therefore, strategies to construct physical barriers to stabilize metal nanoparticles are still in great demand. (ii) Encapsulation with porous material such as oxide;<sup>12,25–27</sup> carbon layers<sup>28–30</sup> and zeolite crystals.<sup>31,32</sup> The catalyst prepared by Arnal *et al.* encapsulating Au in ZrO<sub>2</sub> hollow spheres can achieve 100% CO conversion at 260–280 °C even after a high-temperature treatment of 900 °C.<sup>27</sup> Corma *et al.* reported that the nano-scale Pt species is confined in the pores of the MCM-22 molecular sieve, which can withstand heat treatment up to 540 °C in an air atmosphere. It has better stability performance in the propane dehydrogenation reaction when compared with the catalyst prepared by the usual impregnation method.<sup>31</sup> Compared to the SMSI, encapsulation of metal nanoparticles with porous material indeed enhances the stability of metal nanoparticles due to the construction of physical barriers, which unfortunately reduces the accessible active sites simultaneously. In addition, the preparation process of this type of catalyst is relatively complicated, particularly for the fabrication of nanocage structures, and thus limits its large-scale industrial production. Therefore, it is of considerable interest to develop a simple and effective method to synthesize novel structured support to stabilize metal nanoparticles against sintering.

Gamma alumina is widely used in a variety of industrial processes, including ceramics, petroleum refinement, automobile emission control, *etc.* The  $\gamma$ -Al<sub>2</sub>O<sub>3</sub> supported catalysts are widely used in the industrial catalyst field due to their essential properties of high surface area, good mechanical strength, and chemical and especially thermal stability.<sup>33</sup> However, until now, it has been difficult to find a successful method using  $\gamma$ -Al<sub>2</sub>O<sub>3</sub> to stabilize noble metals including Pt, Pd, and Au, particularly Au nanoparticles, which can anti-sintering at temperatures exceeding 700 °C. Thus, it is still a significant challenge to obtain gamma alumina with the properties mentioned above via a simple and effective strategy.

Au/Al<sub>2</sub>O<sub>3</sub> catalysts show high performance in CO oxidation, catalytic purification of automotive exhausts, elimination of halogenated organic compounds and catalytic combustion of methane.<sup>34–37</sup> However, the resistance to sintering and high dispersion of loaded gold nanocatalysts has been a difficult area of research in this field, particularly for the preparation of highly active gold catalysts using inert alumina as a carrier. Wang *et al.* added Ru as an accelerator to Au/Al<sub>2</sub>O<sub>3</sub> to improve the stability of Au/Al<sub>2</sub>O<sub>3</sub>.<sup>38</sup> Roberto Camposeco *et al.* synthesized Au/TiO<sub>2</sub>-Al<sub>2</sub>O<sub>3</sub> catalysts with a high degree of dispersion, which showed good performance for the oxidation and anti-inactivity of CO.<sup>39</sup> Su *et al.* prepared Au/LaFeO<sub>3</sub>/Al<sub>2</sub>O<sub>3</sub> catalysts.<sup>40</sup> The modification of LaFeO<sub>3</sub> allowed the catalyst to increase its catalytic activity and form larger pores, and also prevented the aggregation and deactivation of gold nanoparticles. Therefore, the preparation of a catalyst with high thermal stability becomes very meaningful work.

Herein, we present a simple and reproducible hydrothermal synthesis method using ammonium oleate as the crystal face protector to synthesize nanorod-shaped porous gamma alumina. Subsequently, the Au/ $\gamma$ -Al<sub>2</sub>O<sub>3</sub> catalyst is prepared by a simple equal-volume impregnation method. Then, we investigated the thermal stability of Au species on different morphology of  $\gamma$ -Al<sub>2</sub>O<sub>3</sub> and surprisingly discovered vastly different sintering resistance behaviors in CO oxidation reaction. It was found that the nanorod-shaped Au/ $\gamma$ -Al<sub>2</sub>O<sub>3</sub> catalyst can achieve 100% CO conversion at 300 °C even after high-temperature annealing at 700 °C, showing excellent thermal stability. It has better stability performance when compared with the catalyst prepared by the commercial gamma alumina under the same conditions. The interaction between the Au nanoparticles and the gamma alumina nanorods was confirmed by XPS, H<sub>2</sub>-TPR, and *in situ* DRIFTS. This study provides another solution for synthesizing catalyst supports capable of effectively stabilizing the metal nanoparticles on its surface. The main text of the article should appear here with headings as appropriate.

## 2 Experimental

### 2.1 Catalysts synthesis

**2.1.1 Preparation of the aluminum sol.** Here, aluminum sol was prepared under acidic conditions by hydrolysis of aluminum isopropoxide. For a typical preparation, a certain amount of aluminum isopropoxide was dissolved in deionized water at 353 K under magnetic stirring and reflux for 1.5 h, while the molar ratio of water to aluminum isopropoxide was 150 : 1. Then, the mixture solution was openly stirred for 1 h at 368 K to evaporate part of the isopropanol. Subsequently, a certain amount of deionized water was added to complement the lost solution, then an appropriate amount of nitric acid (2 mol L<sup>-1</sup>) was added to adjust the pH of the suspension to about 3–4. Finally, the mixture solutions were continuously stirred with a magnetic stirrer at 368 K under condensed reflux for 36 h in preparation for stable transparent aluminum sol.

**2.1.2 Preparation of the  $\gamma$ -Al<sub>2</sub>O<sub>3</sub> nanorods.**  $\gamma$ -Al<sub>2</sub>O<sub>3</sub> nanorods were obtained by a hydrothermal method using ammonium oleate as a crystal surface protector. 7.1 g ammonium oleate and 120 mL aluminum sol (prepared by the above-mentioned method) were dissolved in 70 mL deionized water under magnetic stirring at 353 K for 2 h, then an appropriate amount of ammonia was added into the mixture solution to adjust the pH value to 9. After magnetic stirring for 8 h, the mixture was transferred into a Teflon-lined stainless steel autoclave, heated to 453 K and aged for 72 h. After cooling to room temperature, the solid precipitate was collected by centrifugation, rinsed alternate with water and denatured alcohol several times, and dried in air at 353 K followed by grinding to obtain precursor. Subsequently, the precursor powder was heated at 873 K for 8 h under an air atmosphere to obtain the  $\gamma$ -Al<sub>2</sub>O<sub>3</sub> nanorods, with a heating rate of 5 K min<sup>-1</sup>. The as-prepared  $\gamma$ -Al<sub>2</sub>O<sub>3</sub> nanorods were defined as  $\gamma$ -Al<sub>2</sub>O<sub>3</sub>-r.

**2.1.3 Preparation of the commercial  $\gamma$ -Al<sub>2</sub>O<sub>3</sub>.** For comparison, the commercial  $\gamma$ -Al<sub>2</sub>O<sub>3</sub> with amorphous morphology was

purchased from Aluminum Corporation of China Limited, and heated at 873 K for 8 h under air atmosphere before use. To facilitate the subsequent discussions, it was defined as  $\gamma\text{-Al}_2\text{O}_3\text{-c}$ .

**2.1.4 Preparation of  $\text{Au}/\gamma\text{-Al}_2\text{O}_3$ .** The  $\text{Au}/\gamma\text{-Al}_2\text{O}_3$  catalysts were prepared by equal volume impregnation method. An  $\text{HAuCl}_4$  solution of different concentrations was loaded on two different alumina supports to obtain the required concentration of Au loading. Then, the product was dried at room temperature for 24 h to diffuse it. The product was then washed several times alternately with distilled water and alcohol followed by centrifugal separation and drying under vacuum conditions. Finally, the sample was calcined under air atmosphere at various temperatures (573 K, 973 K) for 4 h. For the convenience of subsequent discussion, the obtained Au catalyst was named  $\text{Au}/\gamma\text{-Al}_2\text{O}_3\text{-r-x}$ , where  $x$  represents the annealing temperature of the gold catalyst. The catalyst supported on commercial alumina was denoted as  $\text{Au}/\gamma\text{-Al}_2\text{O}_3\text{-c-x}$ .

## 2.2 Catalyst characterization

X-ray diffraction (XRD) patterns were obtained using a Phillips X'Pro diffractometer with  $\text{Cu K}\alpha$  ( $\lambda = 1.5418 \text{ \AA}$ ) radiation at 40 kV and 40 mA with  $2\theta$  values between 5 and  $90^\circ$ . The specific surface area was measured on an ASAP-2010 apparatus at liquid nitrogen temperature. The samples were degassed *in vacuo* at 573 K for 6 h before measurement. The Barrett–Joyner–Halenda (BJH) method was used to calculate the pore volume and the pore size distribution. The transmission electron microscopy (TEM) images were collected on a JEOL JEM-200CX instrument at an accelerating voltage of 200 kV. The surface elemental analysis was performed using a Thermo escalate 250XI X-ray photoelectron spectroscopy (XPS) equipped with Al  $\text{K}\alpha$  radiation. C 1s peak at 284.8 eV was used as a calibration peak.

**2.2.1  $\text{H}_2$ -TPR.** Hydrogen temperature-programmed reduction (TPR) experiments were performed using a TP-5080 Adsorption Instrument (Tianjin Xianquan Industry and Trading Co., Ltd.) with a mixed flow of  $\text{H}_2/\text{N}_2$ . In detail, 100 mg of the sample was pretreated at 353 K under Ar flow ( $50 \text{ mL min}^{-1}$ ) for 2 h. The 5%  $\text{H}_2/\text{N}_2$  gas mixture was introduced as a reference flow at a rate of  $50 \text{ mL min}^{-1}$  from room temperature to 873 K ( $10 \text{ K min}^{-1}$ ) and the  $\text{H}_2$  reduction profile was registered with a thermal conductivity detector.

**2.2.2 *In situ* CO-IR.** *In situ* diffuse reflectance infrared Fourier transform spectroscopy (DRIFTS) of CO experiments were carried out in a quartz cell equipped with  $\text{CaF}_2$  windows allowing sample activation and successive measurements in the range of 298–873 K. The catalysts were pressed into a disk located at the center of the cell and activated in the same cell used for the measurement. FT-IR spectra were collected with Bruker Vertex 80v infrared spectrophotometer at a spectra resolution of  $4 \text{ cm}^{-1}$  and accumulation of 64 scans. After  $\text{H}_2$  pretreatment at 573 K for 2 h and He treatment at 303 K for 1 h, the catalyst was scanned to get a background record in  $5 \text{ mL min}^{-1}$  He flow at 303 K. Then, the catalyst was exposed to a CO flow at 303 K for 1 h. IR spectra were recorded at 5 min intervals in 5

$\text{mL min}^{-1}$  He flow at 303 K until there was no signal of gas phase CO while the cell was evacuated.

## 2.3 Evaluation of catalytic performance

In order to investigate the catalytic activity of the catalysts, the CO oxidation reaction was carried out in a laboratory-made fixed bed reactor. The specific steps were as follows: 20 mg of catalyst (20–40 mesh) was added to the reactor, first pretreat with  $\text{N}_2$  at 573 K for 1 h, and the reaction was started after cooling to room temperature. The mixed gas containing CO (2.0% CO, the rest was Ar) and  $\text{O}_2$  were introduced into the fixed bed to start the reaction. The reaction temperature was 323–673 K, and the mixed gas flow rate was  $33 \text{ mL min}^{-1}$ . The reacted product was equipped with a Porapak-Q column gas chromatograph for online analysis.

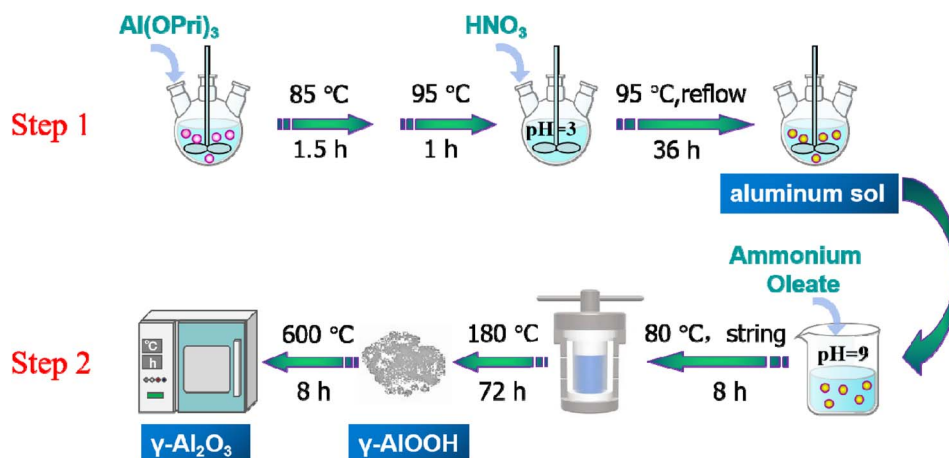
# 3 Results and discussion

## 3.1 Synthesis and characterization of $\text{Au}/\gamma\text{-Al}_2\text{O}_3\text{-r}$ and $\text{Au}/\gamma\text{-Al}_2\text{O}_3\text{-c}$

Alumina was a polymorphic compound,  $\gamma\text{-Al}_2\text{O}_3$  was obtained by calcining boehmite ( $\gamma\text{-AlOOH}$ ) at 500–800  $^\circ\text{C}$ , and its structure was a defective spinel structure. From there, controlling the size and shape of the boehmite nanostructure was the key to alumina's performance and potential applications. In this study, the  $\gamma\text{-Al}_2\text{O}_3$  nanorods were prepared by a two-step synthesis method, the schematic diagram of the preparation of  $\gamma\text{-Al}_2\text{O}_3$  nanorods was shown in Scheme 1. The first step was to prepare aluminum sol by hydrolysis of aluminum isopropoxide under acidic conditions (using nitric acid as a pH adjuster). In the second step, the  $\gamma\text{-Al}_2\text{O}_3$  nanorods were prepared by calcining boehmite precursor at 600  $^\circ\text{C}$ , while the boehmite precursor was produced through a hydrothermal synthesis using ammonia oleate as a topography inducing reagent.

In order to preliminarily explore the formation mechanism of gamma alumina nanorods, we performed XRD characterization of the hydrated products, and the results were shown in Fig. 1(a). It can be seen that the  $2\theta$  angles at  $14.5^\circ$ ,  $28.2^\circ$ ,  $38.3^\circ$ ,  $48.9^\circ$ ,  $55.2^\circ$ ,  $64.03^\circ$  and  $71.9^\circ$  were correspond to the (020), (120), (031), (051), (151), (231) and (251) crystal faces of  $\gamma\text{-AlOOH}$  (JCPDS# 21-1307). Boehmite ( $\gamma\text{-AlOOH}$ ) can be converted to many different forms of alumina through thermal annealing. Therefore, controlling the size and shape of the boehmite precursor was key to improving the properties of the calcined product gamma-alumina. The XRD profiles of the two different alumina and 0.5% Au-loaded catalysts were displayed in Fig. 1(b). It can be seen from the figure that, for all alumina, the  $2\theta$  angles at  $37.4^\circ$ ,  $45.9^\circ$  and  $66.8^\circ$  correspond to the (311), (400) and (440) crystal faces of  $\gamma\text{-Al}_2\text{O}_3$  (JCPDS#29-0063). It can also be seen from the Fig. 1(b) that the prepared alumina has a narrower half-value width and stronger diffraction peak intensity, which indicates that the self-made alumina has better crystallinity than commercial alumina, and also confirms the regularity of its morphology. The XRD of the catalyst loaded with a mass fraction of 0.5% was also shown in Fig. 1(b). It can be





Scheme 1 Schematic illustration of the preparation of the gamma-alumina nanorods.

seen from the figure that when the Au content is low (0.5%), the XRD diffraction peaks of the sample and the XRD characteristic diffraction peaks of the carrier  $\text{Al}_2\text{O}_3$  are consistent, there is no characteristic diffraction peak of Au. This is due to the low loading of Au, which is lower than the detection limit of XRD, and no large particles of Au agglomerated during the roasting process (300 °C). Fig. 1(c) shows the  $\text{N}_2$  adsorption-desorption isotherm and pore distribution of  $\gamma\text{-Al}_2\text{O}_3\text{-r}$  and  $\gamma\text{-Al}_2\text{O}_3\text{-c}$ . The adsorption curves of  $\gamma\text{-Al}_2\text{O}_3\text{-r}$  and  $\gamma\text{-Al}_2\text{O}_3\text{-c}$  are of a typical type IV isotherm with an H3 hysteresis loop, indicating that the two types of alumina have a pore structure. The BET specific surface area of  $\gamma\text{-Al}_2\text{O}_3\text{-r}$  and  $\gamma\text{-Al}_2\text{O}_3\text{-c}$  estimated from this curve was  $103\text{ m}^2\text{ g}^{-1}$  and  $240\text{ m}^2\text{ g}^{-1}$  respectively. Furthermore, the pore

size distribution curve of the two  $\gamma\text{-Al}_2\text{O}_3$  obtained *via* BJH calculations (inset of Fig. 1(c)) reveals that the  $\gamma\text{-Al}_2\text{O}_3\text{-r}$  sample possesses a wide range of pore sizes from 2 to 50 nm with a peaked value at  $\sim 14.5\text{ nm}$ . While the  $\gamma\text{-Al}_2\text{O}_3\text{-c}$  sample possesses a wide range of pore sizes from 2 to 25 nm with a peaked value at  $\sim 5.2\text{ nm}$ .

The morphology of the  $\gamma\text{-Al}_2\text{O}_3\text{-r}$  and  $\gamma\text{-Al}_2\text{O}_3\text{-c}$  are shown in Fig. 2(a) and (b) respectively. The alumina prepared by the hydrothermal method shows a morphology different from that of commercial alumina, as shown in Fig. 2(a). The  $\gamma\text{-Al}_2\text{O}_3\text{-r}$  possesses a nanorod structure with a width of 8–10 nm and a length of 40–120 nm, while the commercial alumina presents the appearance of a porous structure formed by stacking many

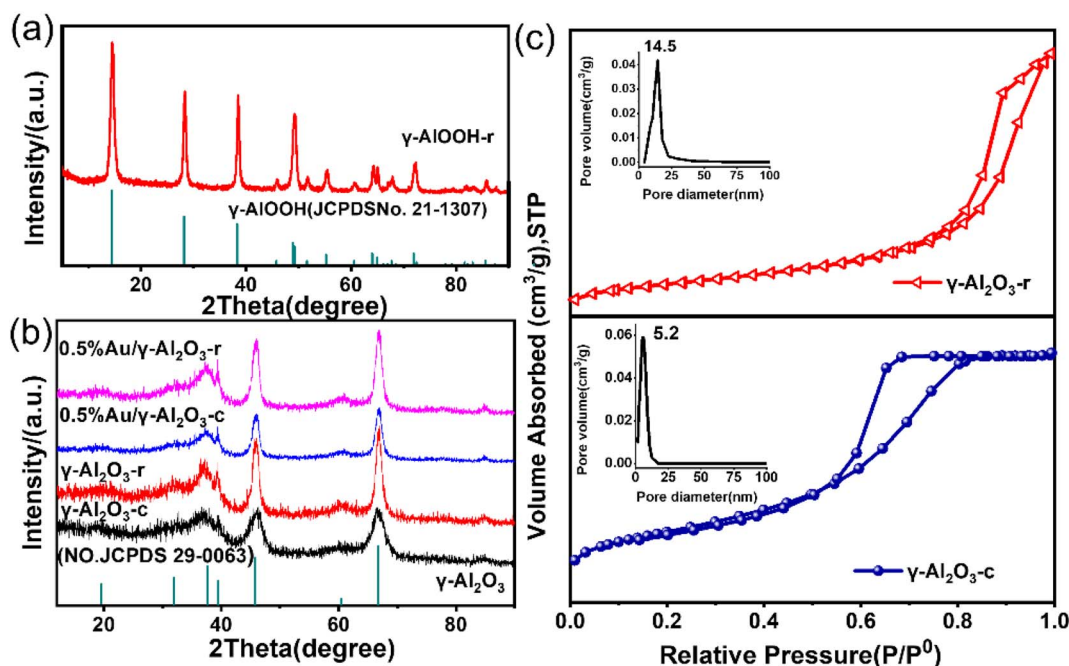


Fig. 1 (a) XRD patterns of  $\gamma\text{-AlOOH-r}$  (b) XRD patterns of as-prepared  $\gamma\text{-Al}_2\text{O}_3\text{-r}$  and  $\gamma\text{-Al}_2\text{O}_3\text{-c}$ ; 0.5%Au/ $\gamma\text{-Al}_2\text{O}_3\text{-r}$  and 0.5%Au/ $\gamma\text{-Al}_2\text{O}_3\text{-c}$ . (c)  $\text{N}_2$  sorption isotherm of  $\gamma\text{-Al}_2\text{O}_3\text{-r}$  and  $\gamma\text{-Al}_2\text{O}_3\text{-c}$ .





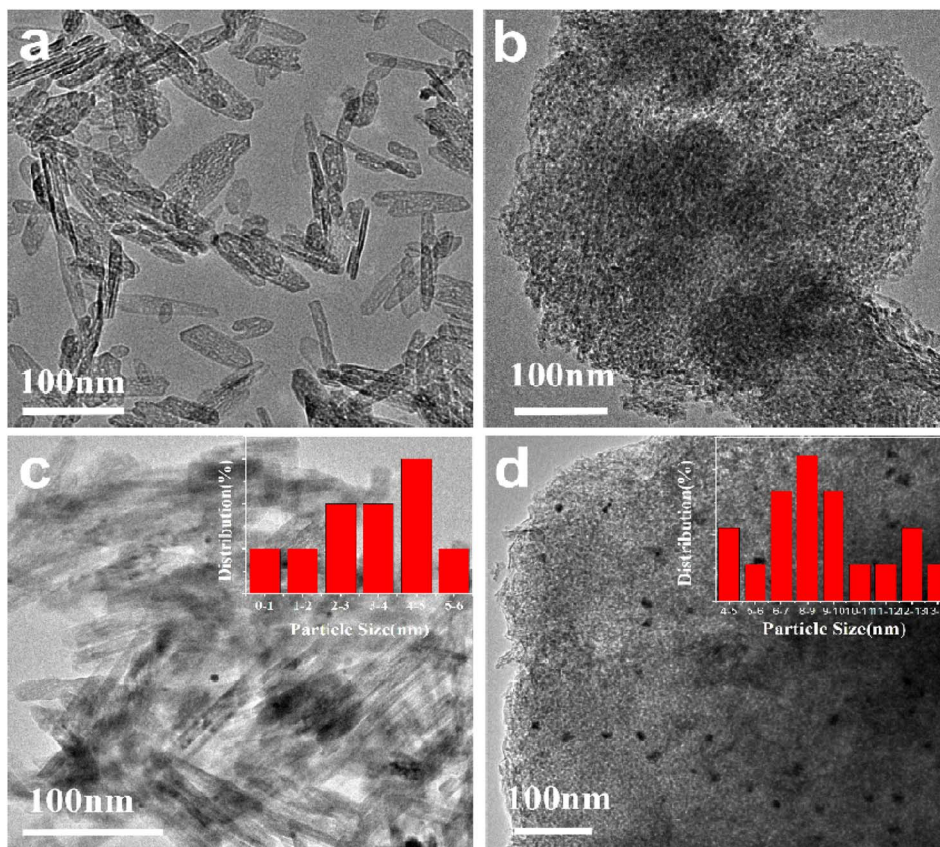


Fig. 2 HRTEM image of the (a)  $\gamma$ - $\text{Al}_2\text{O}_3$ -r; (b)  $\gamma$ - $\text{Al}_2\text{O}_3$ -c; (c) 0.5% $\text{Au}/\gamma$ - $\text{Al}_2\text{O}_3$ -r; (d) 0.5% $\text{Au}/\gamma$ - $\text{Al}_2\text{O}_3$ -c.

small spherical nanoparticles, as shown in Fig. 2(b). The source of the difference in the morphology of the two aluminas is the difference in their synthesis methods, which have undergone a hydrothermal synthesis process. The Au nanoparticles are loaded onto  $\gamma$ - $\text{Al}_2\text{O}_3$ -r and  $\gamma$ - $\text{Al}_2\text{O}_3$ -c *via* equal volume impregnation with a theoretical loading amount of 0.5 wt% and subsequent calcined under air atmosphere at 300 °C for 4 h. Fig. 2(c) and (d) show the TEM images of the 0.5% $\text{Au}/\gamma$ - $\text{Al}_2\text{O}_3$ -r and 0.5% $\text{Au}/\gamma$ - $\text{Al}_2\text{O}_3$ -c catalysts. As shown in Fig. 2(c), it can be seen that the Au nanoparticles on the surface of the  $\gamma$ - $\text{Al}_2\text{O}_3$ -r catalyst are evenly distributed, and the aggregation of metal nanoparticles is not apparent. The size of most Au nanoparticles is below 5 nm (inset of Fig. 2(c)), indicating that the Au nanoparticles are highly dispersed on  $\gamma$ - $\text{Al}_2\text{O}_3$ -r. The dispersibility of Au on  $\gamma$ - $\text{Al}_2\text{O}_3$ -c can be clearly seen in Fig. 2(d), the size of Au nanoparticles is relatively large, with an average size of 8–9 nm (inset of Fig. 2(d)), indicating that using commercial  $\gamma$ - $\text{Al}_2\text{O}_3$  as support, the Au nanoparticles will agglomerate and grow during the calcination process. Therefore, the  $\gamma$ - $\text{Al}_2\text{O}_3$ -r support has better dispersibility for Au nanoparticles than  $\gamma$ - $\text{Al}_2\text{O}_3$ -c support.

### 3.2 Evaluation of CO oxidation performance

As a typical and size-dependent reaction, the oxidation of carbon monoxide (CO) to carbon dioxide ( $\text{CO}_2$ ) is chosen as a simple test reaction to study the activity and thermal stability

of  $\text{Au}/\gamma$ - $\text{Al}_2\text{O}_3$  catalysts, and explore the electron interactions between metal and support due to its special nanorod structure. Fig. 3 shows the CO oxidation performance of the  $\text{Au}/\gamma$ - $\text{Al}_2\text{O}_3$  catalysts calcined at different temperatures. It can be seen from Fig. 3 that whether the catalysts are calcined at 300 °C or 700 °C, the CO oxidation activity of the catalyst with nanorod-shaped  $\gamma$ - $\text{Al}_2\text{O}_3$  as the support was better than that of the catalyst with

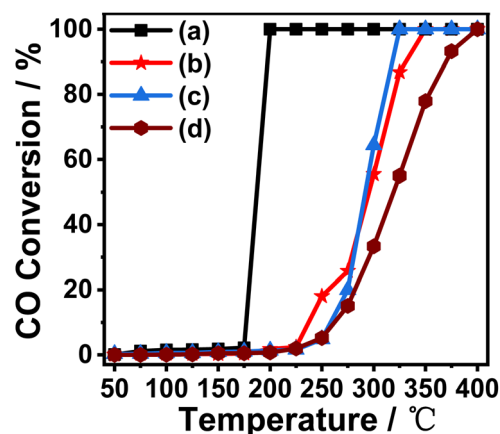


Fig. 3 Catalytic activity of (a) 0.5% $\text{Au}/\gamma$ - $\text{Al}_2\text{O}_3$ -r-300 °C; (b) 0.5% $\text{Au}/\gamma$ - $\text{Al}_2\text{O}_3$ -c-300 °C; (c) 0.5% $\text{Au}/\gamma$ - $\text{Al}_2\text{O}_3$ -r-700 °C; (d) 0.5% $\text{Au}/\gamma$ - $\text{Al}_2\text{O}_3$ -c-700 °C in CO oxidation reaction.



commercial  $\gamma$ - $\text{Al}_2\text{O}_3$  as the support. As shown in Fig. 3, the 0.5% Au/ $\gamma$ - $\text{Al}_2\text{O}_3$ -r catalyst calcined at 300 °C can completely oxidize CO at 175 °C, while the complete conversion temperature of the 0.5% Au/ $\gamma$ - $\text{Al}_2\text{O}_3$ -c catalyst was 350 °C. Previous studies have shown that gold particles with small size and high dispersibility have high CO oxidation activity,<sup>41</sup> and catalysts with small gold particles have high oxidation activity and can completely convert carbon monoxide into carbon dioxide at low temperatures. Therefore, the results of CO oxidation performance are also consistent with the TEM results in Fig. 2(c) and (d). The catalyst with nanorod-shaped  $\gamma$ - $\text{Al}_2\text{O}_3$  as the support has smaller Au particles on the surface, and most of the gold particles are below 5 nm in size, in comparison, the Au nanoparticles on the surface of commercial  $\gamma$ - $\text{Al}_2\text{O}_3$  are larger, with an average size of 8–9 nm.

In order to investigate the thermal stability of the prepared catalysts, we calcined the two prepared catalysts (0.5% Au/ $\gamma$ - $\text{Al}_2\text{O}_3$ -r, 0.5% Au/ $\gamma$ - $\text{Al}_2\text{O}_3$ -c) under air atmosphere at 700 °C for 4 h. The performance of CO oxidation is tested and the results are also shown in Fig. 3. It can be seen from the figure that the catalyst with nanorod-shaped  $\gamma$ - $\text{Al}_2\text{O}_3$  as the support has good thermal stability. The temperature for complete CO conversion was 300 °C, which was much lower than the catalyst with commercial  $\gamma$ - $\text{Al}_2\text{O}_3$  as the support (400 °C). This experimental result shows that the supported Au catalyst prepared with nanorod-shaped  $\gamma$ - $\text{Al}_2\text{O}_3$  as the support has good anti-sintering performance, and even if it was calcined at a high temperature of 700 °C, its surface still has small-sized Au nanoparticles. The supported catalyst with commercial  $\gamma$ - $\text{Al}_2\text{O}_3$  as the support has poor thermal stability. After high-temperature roasting, the Au nanoparticles on the surface will aggregate and sinter, so the catalytic activity was poor.

### 3.3 Characterization of samples after roasting

To further explore the thermal stability of the prepared catalysts, the morphology of the samples after calcined at 700 °C is characterized by TEM, as shown in Fig. 4. Fig. 4(a) shows the

TEM image of the 0.5% Au/ $\gamma$ - $\text{Al}_2\text{O}_3$ -r catalyst after treatment at 700 °C. It can be seen from the figure that its morphology maintains the morphology of  $\gamma$ - $\text{Al}_2\text{O}_3$ -r with an outer diameter of about 8–10 nm and a length of about 40–120 nm, and no obvious agglomerates of the Au nanoparticle can be found. The high-resolution TEM (Fig. 4(b)) shows that the size of the Au particles is about 5 nm, indicating that the Au nanoparticles still have a good dispersion on the surface of the alumina nanorods even after being calcined at a high temperature of 700 °C. Fig. 4(c) shows the TEM image of the 0.5% Au/ $\gamma$ - $\text{Al}_2\text{O}_3$ -c catalyst after calcined at 700 °C. It can clearly see that many agglomerates with darker colors and a small number of large particles are present. The high-resolution TEM (Fig. 4(d)) shows more clearly that the size of the Au particles is about 10 nm, indicating that the Au nanoparticles agglomerated or even partially sintered on the surface of commercial  $\gamma$ - $\text{Al}_2\text{O}_3$  after calcined at 700 °C, which is also the reason for its low CO oxidation performance.

### 3.4 Investigation of the morphology-dependent behaviors of support

High resolution X-ray photoelectron spectroscopy (XPS) was used to explore the effect of the morphology of the  $\gamma$ - $\text{Al}_2\text{O}_3$  support on the metal nanoparticles as well as the chemical states of the Au nanoparticles present in the 0.5% Au/ $\gamma$ - $\text{Al}_2\text{O}_3$ -r and 0.5% Au/ $\gamma$ - $\text{Al}_2\text{O}_3$ -c catalysts after calcined at 700 °C under air atmosphere. As shown in Fig. 5(a), the full scan spectra of the two catalysts clearly show the presence of five peaks assigned to O 1s, C 1s, Al 2s, Au 4f and Al 2p on the surface of both the 0.5% Au/ $\gamma$ - $\text{Al}_2\text{O}_3$ -r and the 0.5% Au/ $\gamma$ - $\text{Al}_2\text{O}_3$ -c catalyst, which indicated that the elemental composition of the surfaces of the two catalysts was the same. To explore the possibility of electronic interactions between Au and  $\gamma$ - $\text{Al}_2\text{O}_3$  support, the spectrum of Au 4f of the two catalysts was shown in Fig. 5(b). For the 0.5% Au/ $\gamma$ - $\text{Al}_2\text{O}_3$ -c catalyst (Fig. 5(b), blue line), the Au 4f spectrum shows two main peaks, and the binding energy (BE) at around 86.8 eV and 83.1 eV following the literature values for 4f 5/2 and Au 4f 7/2 of  $\text{Au}^0$ , respectively,<sup>42</sup> suggesting that Au exists as a metallic phase in the 0.5% Au/ $\gamma$ - $\text{Al}_2\text{O}_3$ -c catalyst. In the case of 0.5% Au/ $\gamma$ - $\text{Al}_2\text{O}_3$ -r catalyst (Fig. 5(b), red line), the Au 4f 5/2 and 4f 7/2 peaks shift to higher BE by approximately 0.2 eV with the binding energy (BE) at around 87.0 eV and 83.3 eV compared to the 0.5% Au/ $\gamma$ - $\text{Al}_2\text{O}_3$ -c catalyst. In this study, whether the composition, the preparation method or the treatment conditions of the two catalysts were the same, the only difference was the support morphology of the two catalysts. Therefore, the positive shift of the 0.5% Au/ $\gamma$ - $\text{Al}_2\text{O}_3$ -r catalyst was due to the interactions between the Au and the special nanorod alumina support. These results clearly show that after calcined at high temperature, there was an electronic interaction between Au and  $\gamma$ - $\text{Al}_2\text{O}_3$ -r support, and Au transfers part of the electrons to the  $\gamma$ - $\text{Al}_2\text{O}_3$ -r support, producing the  $\text{Au}^{\delta+}$  species on the surface of the 0.5% Au/ $\gamma$ - $\text{Al}_2\text{O}_3$ -r catalyst calcined at 700 °C. Furthermore, the experimental results were consistent with this literature.<sup>43</sup> Gaurav Kumar *et al.* using Hammett and DFT studies evaluating differences in the active-site

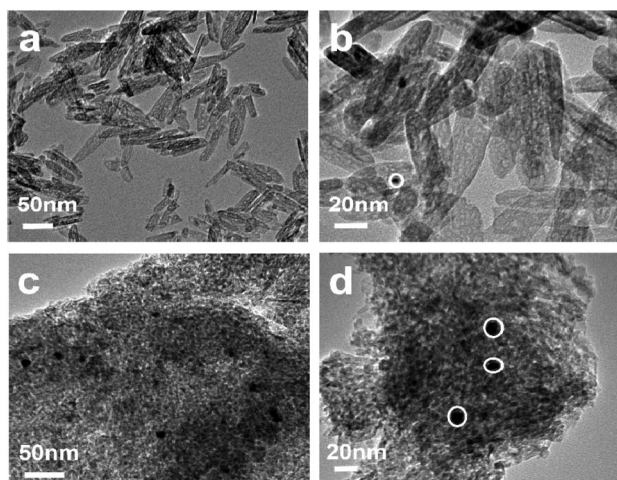


Fig. 4 TEM image of the (a); (b) 0.5% Au/ $\gamma$ - $\text{Al}_2\text{O}_3$ -r (c); (d) 0.5% Au/ $\gamma$ - $\text{Al}_2\text{O}_3$ -c after calcined at 700 °C under air atmosphere.



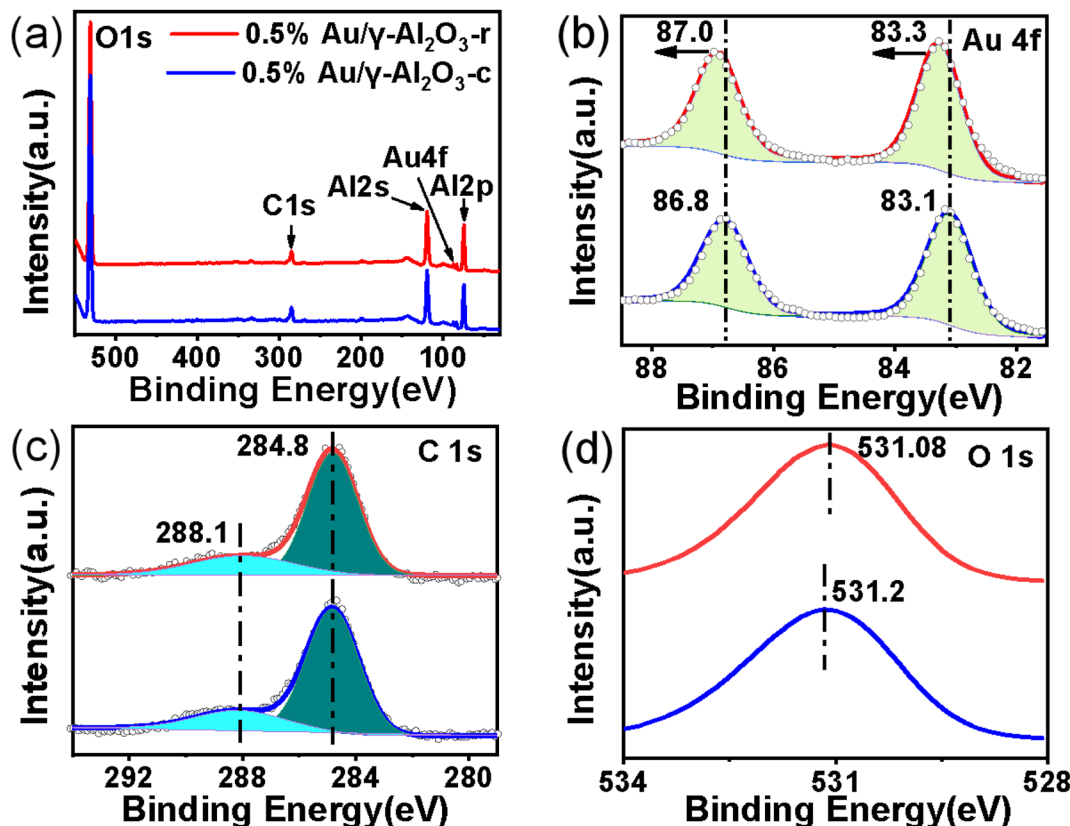


Fig. 5 The XPS spectra of (a) the full scan spectra of 0.5%Au/ $\gamma$ -Al<sub>2</sub>O<sub>3</sub>-r and 0.5%Au/ $\gamma$ -Al<sub>2</sub>O<sub>3</sub>-c after calcined at 700 °C under air atmosphere; (b) Au 4f; (c) C 1s; (d) O 1s.

electronics of supported Au nanoparticle catalysts, and the logical conclusion was that the less active catalysts have more negatively charged Au active sites while the more active catalysts are less negatively (or perhaps more positively) charged. Thus the better CO oxidation activity of the 0.5%Au/ $\gamma$ -Al<sub>2</sub>O<sub>3</sub>-r catalyst may be due to the more positively charged Au species as certified by XPS. Fig. 5(c) shows that the C 1s peak positions of the two catalysts were almost the same. As shown in Fig. 5(d), the O 1s peaks of the 0.5% Au/ $\gamma$ -Al<sub>2</sub>O<sub>3</sub>-c and 0.5% Au/ $\gamma$ -Al<sub>2</sub>O<sub>3</sub>-r catalysts were at about 531.08 eV and 531.2 eV, respectively, and the O 1s peaks could be attributed to the lattice oxygen for  $\gamma$ -Al<sub>2</sub>O<sub>3</sub> that have appeared in the literature.<sup>44</sup> The negative shift of the 0.5% Au/ $\gamma$ -Al<sub>2</sub>O<sub>3</sub>-r catalyst may be due to Au transferring part of the electrons to the  $\gamma$ -Al<sub>2</sub>O<sub>3</sub>-r, the surface of the  $\gamma$ -Al<sub>2</sub>O<sub>3</sub>-r was partially negatively charged. According to the above XPS results, due to the special morphological effect of  $\gamma$ -Al<sub>2</sub>O<sub>3</sub>-r, after calcined at high temperature, there was an electronic interaction between the Au and the  $\gamma$ -Al<sub>2</sub>O<sub>3</sub>-r support, and the Au transfers part of the electrons to the  $\gamma$ -Al<sub>2</sub>O<sub>3</sub>-r support, making it partially positively charged. The partially positively charged Au<sup>δ+</sup> species has higher activity in the CO oxidation reaction, so the Au/ $\gamma$ -Al<sub>2</sub>O<sub>3</sub>-r catalysts show enhanced thermal stabilization.

To further explore the surface chemical properties of the Au on the two  $\gamma$ -Al<sub>2</sub>O<sub>3</sub> supports with different morphology under high calcining temperatures (700 °C), *in situ* DRIFTS was used to measure the adsorbed CO. Fig. 6 compares IR spectra of CO

adsorbed on the 0.5%Au/ $\gamma$ -Al<sub>2</sub>O<sub>3</sub>-r and 0.5%Au/ $\gamma$ -Al<sub>2</sub>O<sub>3</sub>-c catalysts. As shown in Fig. 6 (blue line), two bands were detected on the 0.5%Au/ $\gamma$ -Al<sub>2</sub>O<sub>3</sub>-c catalyst at 2200 and 2088 cm<sup>-1</sup>, respectively. The former was attributed to CO adsorbed on cationic gold (Au(I) or Au(III)).<sup>45</sup> The latter belonged to two linear CO species adsorbed on the metallic Au sites.<sup>46</sup> In comparison with the Au-supported catalyst on commercial  $\gamma$ -Al<sub>2</sub>O<sub>3</sub>, adsorptions of CO on the 0.5%Au/ $\gamma$ -Al<sub>2</sub>O<sub>3</sub>-r catalyst (Fig. 6, red line) result in the appearance of two bands at 2206 and 2100 cm<sup>-1</sup>, which can

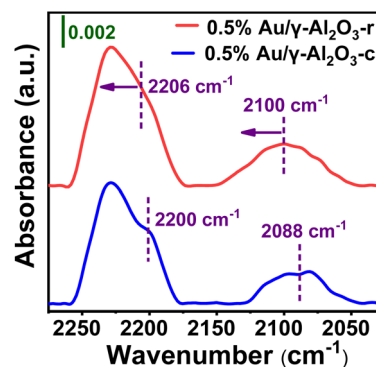


Fig. 6 *In situ* DRIFT spectra of CO adsorption on 0.5%Au/ $\gamma$ -Al<sub>2</sub>O<sub>3</sub>-r (red line) and 0.5%Au/ $\gamma$ -Al<sub>2</sub>O<sub>3</sub>-c (blue line) after calcined at 700 °C under air atmosphere.





also be assigned to CO adsorbed on cationic gold (Au(I) or Au(III)) and the metallic Au sites respectively. In addition, there was a blue shift (*ca.* 12 cm<sup>-1</sup>) on the 0.5%Au/ $\gamma$ -Al<sub>2</sub>O<sub>3</sub>-r catalysts, which was a result of the electronic modification, and corresponds to a formally positively charged Au, the blue shift of the CO adsorption band may be attributed to electron withdrawing from Au NPs to  $\gamma$ -Al<sub>2</sub>O<sub>3</sub>-r support. The DRIFTS measurements show the presence of Au<sup>δ+</sup> species on the surface of 0.5%Au/ $\gamma$ -Al<sub>2</sub>O<sub>3</sub>-r catalyst after calcined at 700 °C, which was consistent with the results of XPS (Fig. 5). These characterization results further confirm that there was electronic interaction between the Au nanoparticles and the special nanorod-like gamma alumina support after being calcined under high temperature, which resulted in better anti-sintering performance.

The redox performance was a critical parameter during deep oxidation reactions such as CO oxidation reaction, which was usually investigated by H<sub>2</sub>-TPR. In order to determine the reduction characteristics of Au/ $\gamma$ -Al<sub>2</sub>O<sub>3</sub> catalysts at different morphology and calcination temperatures, we performed H<sub>2</sub>-TPR experiments. The 100 mg sample was pretreated with a stream of argon gas (50 mL min<sup>-1</sup>) at 353 K for 2 h. The H<sub>2</sub> reduction curve was recorded with a thermal conductivity detector using a 5% H<sub>2</sub>/N<sub>2</sub> mixture as a reference stream introduced from room temperature to 823 K (10 K min<sup>-1</sup>) at a 50 mL min<sup>-1</sup> rate. As shown in Fig. 7, the H<sub>2</sub>-TPR plots show the characteristic peaks of the Au/ $\gamma$ -Al<sub>2</sub>O<sub>3</sub> catalysts over the temperature range from 297 K to 823 K. In both Au/ $\gamma$ -Al<sub>2</sub>O<sub>3</sub> catalysts, similar H<sub>2</sub> consumption profiles were showed observed, in which a single peak existed at about 334 K for the 0.5%Au/ $\gamma$ -Al<sub>2</sub>O<sub>3</sub>-r catalyst and around 361 K for the 0.5%Au/ $\gamma$ -Al<sub>2</sub>O<sub>3</sub>-c catalyst. The peak was attributed to oxygen included in gold oxide (AuO<sub>x</sub>) on  $\gamma$ -Al<sub>2</sub>O<sub>3</sub>-r and  $\gamma$ -Al<sub>2</sub>O<sub>3</sub>-c.<sup>47,48</sup> Considering the low-temperature peaks (334 K and 361 K) of the Au/ $\gamma$ -Al<sub>2</sub>O<sub>3</sub> catalysts, the Au nanoparticles on the  $\gamma$ -Al<sub>2</sub>O<sub>3</sub> support contained some oxygen content that can be used for the oxidation of CO. Furthermore, whether calcined at 300 °C or 700 °C, the peak of the Au/ $\gamma$ -Al<sub>2</sub>O<sub>3</sub>-r catalyst appeared at a temperature around 30 K lower than that of the Au/ $\gamma$ -Al<sub>2</sub>O<sub>3</sub>-c catalyst,

confirming that the oxygen species of gold oxide on  $\gamma$ -Al<sub>2</sub>O<sub>3</sub> nanorod were more active concerning oxidation of reductant than the oxygen content of gold oxide on commercial  $\gamma$ -Al<sub>2</sub>O<sub>3</sub>. Combined with the results of activity evaluation, the lower the reduction peak temperature, the better the activity, which can be attributed to the reduction peak of active gold oxide species. The result of H<sub>2</sub>-TPR was also consistent with the results of CO catalytic oxidation, with the gold supported on  $\gamma$ -Al<sub>2</sub>O<sub>3</sub> nanorods having better catalytic activity. The H<sub>2</sub>-TPR results of the catalysts calcined at different temperatures showed that the area of the low-temperature reduction peak became smaller after high-temperature calcination (700 °C). Combined with the activity evaluation results, the larger the reduction peak area, the better the activity. Take the 0.5%Au/ $\gamma$ -Al<sub>2</sub>O<sub>3</sub>-r catalyst as an example, the 0.5%Au/ $\gamma$ -Al<sub>2</sub>O<sub>3</sub>-r-300 °C catalyst has a larger reduction peak area than that of 0.5%Au/ $\gamma$ -Al<sub>2</sub>O<sub>3</sub>-r-700 °C, which means that there were more active oxide species, so its activity was better. In addition, the difference between the peak types of the two catalysts can also be clearly seen in Fig. 7. The reduction peak of the 0.5%Au/ $\gamma$ -Al<sub>2</sub>O<sub>3</sub>-r catalyst was narrow, while the reduction peak of the 0.5%Au/ $\gamma$ -Al<sub>2</sub>O<sub>3</sub>-c catalyst was broader. According to the literature,<sup>49</sup> the particle size distribution of metal particles on the catalyst surface with a narrow reduction peak was uniform. The reason was that the diffusion and adsorption properties of hydrogen were similar, and the reduction process will proceed simultaneously, so the peak was narrow. Whereas the species corresponding to broad reduction peaks have different properties. This result was consistent with our previous TEM characterization results (Fig. 2 and 4). The Au dispersion on the surface of the gamma alumina nanorods was more uniform, which may be related to the regular morphology of the alumina support. To sum up, the results of H<sub>2</sub>-TPR further confirmed the morphology-dependent effects of the gamma alumina support. The active gold species of the catalyst supported by  $\gamma$ -Al<sub>2</sub>O<sub>3</sub> nanorods were more easily reduced and thus have higher activity in CO oxidation reaction. The interaction between the  $\gamma$ -Al<sub>2</sub>O<sub>3</sub> nanorods support and Au can prevent the aggregation and growth of the Au nanoparticles at high temperature, so it has better thermal stability.

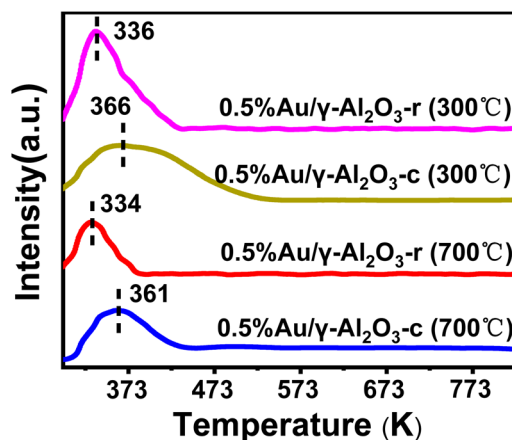


Fig. 7 H<sub>2</sub>-TPR profiles of 0.5%Au/ $\gamma$ -Al<sub>2</sub>O<sub>3</sub> catalysts with different shapes and calcination temperatures.

## 4 Conclusions

The nanorods gamma alumina with regular and uniform morphology has been synthesized *via* a simple hydrothermal synthesis method. The special morphology of the alumina support and interfacial interactions are responsible for stabilizing Au nanoparticles at high temperatures. The morphology of the support, that is, the exposed crystal facets, can influence the catalytic performance through metal-support interactions (MSI). A charge transfer from the Au nanoparticles to the  $\gamma$ -Al<sub>2</sub>O<sub>3</sub> nanorods was observed by XPS, CO-DRIFTS and H<sub>2</sub>-TPR characterization and higher thermal stability in CO oxidation was observed as compared to Au on commercial  $\gamma$ -Al<sub>2</sub>O<sub>3</sub>. Even after calcination at 700 °C, higher stability and excellent catalytic activity can be achieved, which further confirm the small size and high dispersion of Au nanoparticles. Therefore, this finding reveals the distinct morphology-dependent behaviors of



$\gamma$ -Al<sub>2</sub>O<sub>3</sub>. The nanorod-shaped gamma alumina can stabilize the Au nanoparticles against sintering through the MSI, and such a strategy of tuning the catalyst performance by modulating the morphology of the support can be used to guide the synthesis of other thermally stable catalysts.

## Author contributions

W. C. and L. F. conceived the work. W. C. and X. S. designed the experiments and wrote the paper. W. C., X. S. and Y. B. performed the experiments. A. L. and J. G. helped perform the analysis with constructive discussions. K. H. guided the work. All authors discussed the results.

## Conflicts of interest

There are no conflicts to declare.

## Acknowledgements

This work was funded by the National Natural Science Foundation of China (52075144); University Natural Sciences Research Project of Anhui Province (Project Number: 2022AH051802) and the Anhui Province Key Research and Development Program (202104a05020065).

## Notes and references

- 1 P. Biloen, J. N. Helle, H. Verbeek, F. M. Dautzenberg and W. Sachtler, *J. Catal.*, 1980, **63**, 112–118.
- 2 G. X. Pei, X. Y. Liu, X. Yang, L. Zhang, A. Wang, L. Li, H. Wang, X. Wang and T. Zhang, *ACS Catal.*, 2017, **7**, 1491–1500.
- 3 H. Tang, J. Wei, F. Liu, B. Qiao, X. Pan, L. Li, J. Liu, J. Wang and T. Zhang, *J. Am. Chem. Soc.*, 2015, jacs.5b11306.
- 4 K. An, S. Alayoglu, N. Musselwhite, K. Na and G. A. Somorjai, *J. Am. Chem. Soc.*, 2014, **136**, 6830–6833.
- 5 H. Guan, Y. Chen, C. Ruan, J. Lin, Y. Su, X. Wang and L. Qu, *Chin. J. Catal.*, 2020, **41**, 613–621.
- 6 B. Qiao, J. Lin, A. Wang, Y. Chen, T. Zhang and J. Liu, *Chin. J. Catal.*, 2015, **36**, 1505–1511.
- 7 A. Corma and H. Garcia, *Chem. Soc. Rev.*, 2008, **37**, 2096–2126.
- 8 D. I. Enache, J. K. Edwards, P. Landon, B. Solsona-Espriu, A. F. Carley, A. A. Herzing, M. Watanabe, C. J. Kiely, D. W. Knight and G. J. Hutchings, *Science*, 2006, **311**, 362–365.
- 9 M. Yang, S. Li, Y. Wang, J. A. Herron, Y. Xu, L. F. Allard, S. Lee, J. Huang, M. Mavrikakis and M. Flytzani-Stephanopoulos, *Science*, 2014, **346**, 1498–1501.
- 10 Y. Nosaka and A. Y. Nosaka, *Chem. Rev.*, 2017, **117**, 11302–11336.
- 11 S. Liu, W. Xu, Y. Niu, B. Zhang, L. Zheng, W. Liu, L. Li and J. Wang, *Nat. Commun.*, 2019, **10**, 5790.
- 12 J. Lu, B. Fu, M. C. Kung, G. Xiao, J. W. Elam, H. H. Kung and P. C. Stair, *Science*, 2012, **335**, 1205–1208.
- 13 E. Wolf and F. Alfani, *Catal. Rev.*, 1982, **24**, 329–371.
- 14 J. Radnik, A. Benhmid, V. N. Kalevaru, M. M. Pohl, A. Martin, B. Lücke and U. Dingerdissen, *Angew. Chem., Int. Ed.*, 2005, **44**, 6771–6774.
- 15 J. Zhang, H. Wang, L. Wang, S. Ali, C. Wang, L. Wang, X. Meng, B. Li, D. S. Su and F.-S. Xiao, *J. Am. Chem. Soc.*, 2019, **141**, 2975–2983.
- 16 Y. Yao, Z. Huang, P. Xie, L. Wu, L. Ma, T. Li, Z. Pang, M. Jiao, Z. Liang and J. Gao, *Nat. Nanotechnol.*, 2019, **14**, 851–857.
- 17 S. Zhang, P. N. Plessow, J. J. Willis, S. Dai, M. Xu, G. W. Graham, M. Cargnello, F. Abild-Pedersen and X. Pan, *Nano Lett.*, 2016, **16**, 4528–4534.
- 18 M. Xu, S. He, H. Chen, G. Cui, L. Zheng, B. Wang and M. Wei, *ACS Catal.*, 2017, **7**, 7600–7609.
- 19 H. Y. Kim, H. M. Lee and G. Henkelman, *J. Am. Chem. Soc.*, 2012, **134**, 1560–1570.
- 20 H. Ha, S. Yoon, K. An and H. Y. Kim, *ACS Catal.*, 2018, **8**, 11491–11501.
- 21 J. Jones, H. Xiong, A. T. DeLaRiva, E. J. Peterson, H. Pham, S. R. Challa, G. Qi, S. Oh, M. H. Wiebenga and X. I. Pereira Hernández, *Science*, 2016, **353**, 150–154.
- 22 J. Kašpar, P. Fornasiero and M. Graziani, *Catal. Today*, 1999, **50**, 285–298.
- 23 S. Carrettin, P. Concepción, A. Corma, J. M. López Nieto and V. F. Puentes, *Angew. Chem., Int. Ed.*, 2004, **43**, 2538–2540.
- 24 C. T. Campbell and C. H. Peden, *Science*, 2005, **309**, 713–714.
- 25 Z. Gao and Y. Qin, *Acc. Chem. Res.*, 2017, **50**, 2309–2316.
- 26 J. Huo, J.-P. Tessonnier and B. H. Shanks, *ACS Catal.*, 2021, **11**, 5248–5270.
- 27 P. M. Arnal, M. Comotti and F. Schüth, *Angew. Chem., Int. Ed.*, 2006, **45**, 8224–8227.
- 28 W. Zhan, Y. Shu, Y. Sheng, H. Zhu, Y. Guo, L. Wang, Y. Guo, J. Zhang, G. Lu and S. Dai, *Angew. Chem., Int. Ed.*, 2017, **56**, 4494–4498.
- 29 W. Chen, Z. Fan, X. Pan and X. Bao, *J. Am. Chem. Soc.*, 2008, **130**, 9414–9419.
- 30 Y. Wu, *Angew. Chem., Int. Ed.*, 2019, **58**, 18388–18393.
- 31 A. Corma, *Chem. Rev.*, 1997, **97**, 2373–2420.
- 32 P. Munnik, P. E. De Jongh and K. P. De Jong, *J. Am. Chem. Soc.*, 2014, **136**, 7333–7340.
- 33 K. Murata, Y. Mahara, J. Ohyama, Y. Yamamoto, S. Arai and A. Satsuma, *Angew. Chem.*, 2017, **129**, 16209–16213.
- 34 B. Qiao, J. Lin, A. Wang and Y. Chen, *Chin. J. Catal.*, 2015, **36**(9), 1505–1511.
- 35 T. Chaieb, L. Delannoy, S. Casale, C. Louis and C. Thomas, *Chem. Commun.*, 2015, **51**, 796–799.
- 36 F. Cárdenas-Lizana, S. Gómez-Quero, A. Hugon, L. Delannoy, C. Louis and M. A. Keane, *J. Catal.*, 2009, **262**, 235–243.
- 37 S. Yao, Z. Chen, S. Weng, L. Mao, X. Zhang, J. Han, Z. Wu, H. Lu, X. Tang and B. Jiang, *J. Hazard. Mater.*, 2019, **373**, 698–704.
- 38 X. Wang, G. Lu, Y. Guo, Z. Zhang and Y. Guo, *Environ. Chem. Lett.*, 2011, **9**, 185–189.
- 39 R. Camposeco and R. Zanella, *Environ. Sci. Pollut. Res.*, 2022, **29**, 76992–77006.
- 40 H. Su, Y. Zheng, X. Sun, L. Sun, X. Xu and C. Qi, *Kinet. Catal.*, 2020, **61**, 304–309.



- 41 R. Grisel, C. Weststrate, A. Goossens, M. Crajé, A. Van der Kraan and B. Nieuwenhuys, *Catal. Today*, 2002, **72**, 123–132.
- 42 Z. Huo, C.-k. Tsung, W. Huang, X. Zhang and P. Yang, *Nano Lett.*, 2008, **8**, 2041–2044.
- 43 G. Kumar, L. Tibbitts, J. Newell, B. Panthi, A. Mukhopadhyay, R. M. Rioux, C. J. Pursell, M. Janik and B. D. Chandler, *Nat. Chem.*, 2018, **10**, 268–274.
- 44 B. R. Strohmeier, *Surf. Sci. Spectra*, 1994, **3**, 135–140.
- 45 N. Parkyns, *J. Phys. Chem.*, 1971, **75**, 526–531.
- 46 E. Roze, P. Gravejat, E. Quinet, J. L. Rousset and D. Bianchi, *J. Phys. Chem. C*, 2009, **113**, 1037–1045.
- 47 S.-Y. Lai, Y. Qiu and S. Wang, *J. Catal.*, 2006, **237**, 303–313.
- 48 M. J. Kim, G.-H. Han, S. H. Lee, H. W. Jung, J. W. Choung, C. H. Kim and K.-Y. Lee, *J. Hazard. Mater.*, 2020, **384**, 121341.
- 49 X. Tang, B. Zhang, Y. Li, Y. Xu, Q. Xin and W. Shen, *Catal. Lett.*, 2004, **97**, 163–169.

